

# Small-Scale Spatial-Temporal Correlation Modeling for Reconfigurable Intelligent Surfaces

Shu Sun and Hangsong Yan

## Abstract

The reconfigurable intelligent surface (RIS) is an emerging promising candidate technology for the sixth-generation wireless networks, where the element spacing is usually of sub-wavelength. Only limited knowledge, however, has been gained about the spatial-temporal correlation behavior among the elements in an RIS. In this paper, we investigate the joint spatial-temporal correlation models for an RIS in a wireless communication system. Joint small-scale spatial-temporal correlation functions are provided and analyzed for both ideal isotropic scattering and more practical non-isotropic scattering environments, where the latter is studied by employing an angular distribution derived from real-world millimeter-wave measurements. Analytical and simulation results demonstrate that the joint spatial-temporal correlation can be represented by a four-dimensional sinc function under isotropic scattering, while the correlation is generally stronger with more fluctuation and significantly fewer dominant channel eigenvalues for non-isotropic scattering.

## Index Terms

Channel model, reconfigurable intelligent surface (RIS), small-scale fading, spatial-temporal correlation.

## I. INTRODUCTION

Massive MIMO [1] is one of the key enabling technologies for the fifth-generation (5G) wireless communications, which can bring tremendous advantages in spectral efficiency, energy efficiency, and power control [2]–[5]. As a natural extension of Massive MIMO, more elements may be arranged in a small form factor if the element spacing further decreases from the half-wavelength, so as to realize super directivity and high-efficient power transfer [6]. The entire array can be regarded as a spatially-continuous electromagnetic aperture in its ultimate form [7]. This

type of extended Massive MIMO is named Holographic MIMO [7], [8]. Meanwhile, analogous to the metasurface concept in the optical domain [9], [10], the sub-wavelength architecture has the potential to manipulate impinging electromagnetic waves through reflection, scattering, refraction, polarization transformation, among other functionalities, for wireless communication purposes. Therefore, such sort of structure is also referred to as reconfigurable intelligent surface (RIS) [11], [12], large intelligent surface [13], etc. In this paper, we use RIS as the blanket term for all the aforementioned two-dimensional sub-wavelength architectures. In order to unleash the full potentials of the RIS technology, it is necessary to understand its fundamental properties, among which the associated channel model is of paramount importance since it is the foundation of a variety of aspects including deployment decision, algorithm selection, and performance evaluation [14]–[17].

Despite the upsurge in research interests of RIS, only limited works are available in the open literature on characterizing its channel model. The large-scale free space path loss model for RIS-assisted wireless communications has been proposed in [18] whereas the small-scale fading investigation is ongoing. A parametric channel model for RIS-empowered systems has been presented in [19], but without explicit and tractable expressions for the small-scale fading. The authors of [7] have studied the small-scale fading of RIS via wave propagation theories and established a Fourier plane-wave spectral representation of the three-dimensional (3D) stationary small-scale fading. In [20], a spatially-correlated Rayleigh fading model has been derived under isotropic scattering. Nevertheless, the works in [7], [20] did not consider the temporal correlation among RIS elements. To fill in this gap, this paper explores the joint spatial-temporal correlation models for RIS under both isotropic and non-isotropic scattering. Specifically, a closed-form four-dimensional (4D) sinc function is derived to describe the joint spatial-temporal correlation in the isotropic scattering environment. For the more practical non-isotropic scattering, we utilize a realistic 3D angular distribution extracted from extensive real-world millimeter-wave (mmWave) propagation measurements in the urban micro scenario [15], [21]–[23]. The joint spatial-temporal correlation behaviors with various motion directions are unveiled through simulations.

## II. SYSTEM MODEL

We consider an RIS equipped with  $N$  elements in a wireless communication system, where the RIS can act as a transmitter, receiver, or interacting object in the propagation environment and can translate in the 3D space. For the purpose of exposition, we focus on the reception

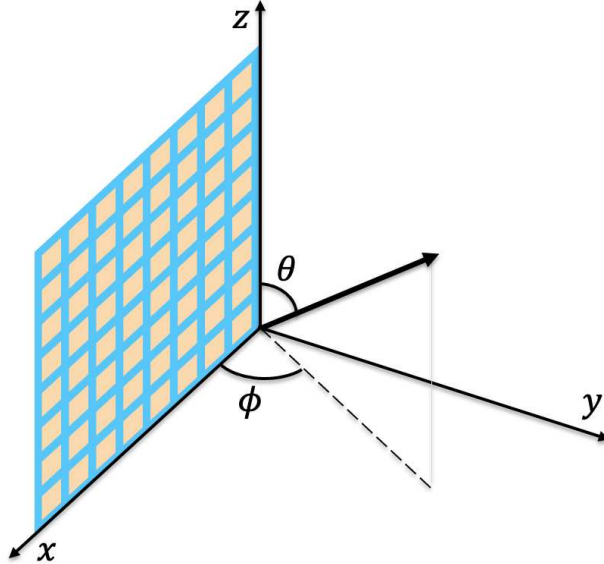


Fig. 1: The orientation of an RIS with the associated coordinate system, where  $\phi$  and  $\theta$  denote the azimuth and zenith angles, respectively.

mode of the RIS in this paper, but the resultant spatial-temporal correlation models have more general applicability. The coordinate system and definitions of azimuth and zenith angles herein are aligned with the 3GPP TR 38.901 [24], as illustrated in Fig. 1. Without loss of generality, the RIS is assumed to be located in the  $xz$  plane, where its horizontal and vertical lengths are  $L_x$  and  $L_z$ , respectively. The motion direction of the RIS is described jointly by the azimuth angle  $\varphi$  and zenith angle  $\vartheta$  with a moving speed of  $\|\mathbf{v}\|$ , where

$$\mathbf{v} = v[\cos\varphi\sin\vartheta, \sin\varphi\sin\vartheta, \cos\vartheta]^T \quad (1)$$

When there are  $P$  plane waves impinging on the RIS at time instant  $t$ , the channel at the RIS can be expressed as

$$\mathbf{h}(t) = \sqrt{\frac{N}{P}} \sum_{p=1}^P \alpha_p \mathbf{a}(\phi_p, \theta_p) e^{j\frac{2\pi}{\lambda} \mathbf{v}^T \mathbf{e}_p t} \quad (2)$$

where  $\alpha_p$  and  $\phi_p(\theta_p)$  denote the complex gain and azimuth (zenith) angle of arrival (AoA) of the  $p$ -th plane wave, respectively,  $\mathbf{e}_p = [\cos\phi\sin\theta, \sin\phi\sin\theta, \cos\theta]^T$ . Additionally,  $\mathbf{a}$  denotes the array response vector at the RIS, which is given by

$$\mathbf{a}(\phi, \theta) = \frac{1}{\sqrt{N}} \left[ 1, \dots, e^{j\frac{2\pi}{\lambda} (x(n)d_x \cos\phi \sin\theta + z(n)d_z \cos\theta)}, \dots, e^{j\frac{2\pi}{\lambda} (x(N)d_x \cos\phi \sin\theta + z(N)d_z \cos\theta)} \right]^T \quad (3)$$

where  $d_x$  and  $d_z$  are the adjacent element spacing of the RIS in the  $x$  and  $z$  directions, respectively.  $x(n)$  and  $z(n)$  are respectively the element indices in the horizontal and vertical directions, which are calculated as

$$x(n) = \text{mod}(n - 1, N_x), z(n) = \lfloor (n - 1)/N_x \rfloor \quad (4)$$

with  $N_x$  denoting the number of elements per row. Denote the average attenuation of the  $P$  plane waves as  $\mu$ , then as  $P \rightarrow \infty$ , based on the central limit theorem, the normalized spatial-temporal correlation matrix  $\mathbf{R}(\tau)$  is given by

$$\mathbf{R}(\tau) = \frac{1}{\mu} \mathbb{E} \left\{ \mathbf{h}(t) \mathbf{h}^H(t + \tau) \right\} \quad (5)$$

Since  $P \rightarrow \infty$ , the discrete random variables  $\phi_p$  and  $\theta_p$  become continuous random variables  $\phi$  and  $\theta$ , which are characterized by a certain angular distribution  $f(\phi, \theta)$ . Consequently, the  $(m, n)$ -th element of  $\mathbf{R}(\tau)$  can be characterized as

$$\begin{aligned} [\mathbf{R}(\tau)]_{m,n} &= N \mathbb{E} \left\{ [\mathbf{a}(\phi, \theta)]_{m,n} [\mathbf{a}^H(\phi, \theta)]_{m,n} e^{-j\frac{2\pi}{\lambda} \tau \mathbf{v}^T \mathbf{e}_p} \right\} \\ &= \mathbb{E} \left\{ e^{j\frac{2\pi}{\lambda} [(x(m) - x(n))d_x \cos \phi \sin \theta + (z(m) - z(n))d_z \cos \theta]} e^{-j\frac{2\pi}{\lambda} \tau (\cos \phi \sin \theta \cos \varphi \sin \vartheta + \sin \phi \sin \theta \sin \varphi \sin \vartheta + \cos \theta \cos \vartheta)} \right\} \\ &= \int_0^\pi \int_0^\pi \left\{ e^{j\frac{2\pi}{\lambda} [(x(m) - x(n))d_x - \tau \cos \varphi \sin \vartheta] \cos \phi \sin \theta - \tau \sin \varphi \sin \vartheta \sin \phi \sin \theta + ((z(m) - z(n))d_z - \tau \cos \vartheta) \cos \theta} \right. \\ &\quad \left. \times f(\phi, \theta) \right\} d\phi d\theta, \quad m, n = 1, \dots, N \end{aligned} \quad (6)$$

In the next two sections, we will conduct further explorations of  $\mathbf{R}(\tau)$  under both isotropic and non-isotropic scattering circumstances.

### III. ISOTROPIC SCATTERING

For the isotropic scattering environment, the angular distribution function is expressed as

$$f(\phi, \theta) = \frac{\sin \theta}{2\pi}, \quad \theta \in [0, \pi], \quad \varphi \in [0, \pi] \quad (7)$$

Thus (6) can be recast as

$$\begin{aligned} [\mathbf{R}(\tau)]_{m,n} &= \frac{1}{2\pi} \int_0^\pi \int_0^\pi \left\{ e^{j\frac{2\pi}{\lambda} [(x(m) - x(n))d_x - \tau \cos \varphi \sin \vartheta] \cos \phi \sin \theta - \tau \sin \varphi \sin \vartheta \sin \phi \sin \theta + ((z(m) - z(n))d_z - \tau \cos \vartheta) \cos \theta} \right. \\ &\quad \left. \times \sin \theta \right\} d\phi d\theta, \quad m, n = 1, \dots, N \end{aligned} \quad (8)$$

**Proposition 1.** With isotropic scattering in the half-space in front of the RIS, the joint spatial-temporal correlation matrix  $\mathbf{R}(\tau)$  is given by

$$[\mathbf{R}(\tau)]_{m,n} = \text{sinc}\left(\frac{2\|\mathbf{d}_m - \mathbf{d}_n - \tau\mathbf{v}\|}{\lambda}\right), \quad m, n = 1, \dots, N \quad (9)$$

where  $\text{sinc}(x) = \frac{\sin(\pi x)}{\pi x}$  is the sinc function,  $\mathbf{d}_m$  and  $\mathbf{d}_n$  denote the coordinates of the  $m$ -th and  $n$ -th RIS element, respectively, and  $\mathbf{v}$  is provided in (1).

*Proof:* It is noteworthy that (8) applies when the RIS is located parallel with the  $xz$  plane, so that the  $y$  coordinate of any RIS element is the same hence canceled out when subtracting one from another. Nevertheless, in more general cases where the RIS is arbitrarily oriented, (8) can be extended to

$$\begin{aligned} [\mathbf{R}(\tau)]_{m,n} = & \frac{1}{2\pi} \int_0^\pi \int_0^\pi \left\{ \exp \left( j \frac{2\pi}{\lambda} [((x(m) - x(n))d_x - v\tau \cos\varphi \sin\vartheta) \cos\phi \sin\theta \right. \right. \\ & \left. \left. ((y(m) - y(n))d_y - v\tau \sin\varphi \sin\vartheta) \sin\phi \sin\theta + ((z(m) - z(n))d_z - v\tau \cos\vartheta) \cos\theta] \right) \right. \\ & \left. \times \sin\theta \right\} d\phi d\theta \end{aligned} \quad (10)$$

Due to the isotropy of the scattering environment, the RIS can be rotated to result in a new set of coordinates  $\{\tilde{x}(n), \tilde{y}(n), \tilde{z}(n), \tilde{d}_x, \tilde{d}_y, \tilde{d}_z\}$ , based on which (10) can be transformed to

$$\begin{aligned} [\mathbf{R}(\tau)]_{m,n} = & \frac{1}{2\pi} \int_0^\pi \int_0^\pi \left\{ \exp \left( j \frac{2\pi}{\lambda} [((\tilde{x}(m) - \tilde{x}(n))\tilde{d}_x - v\tau \cos\varphi \sin\vartheta) \cos\phi \sin\theta \right. \right. \\ & \left. \left. ((\tilde{y}(m) - \tilde{y}(n))\tilde{d}_y - v\tau \sin\varphi \sin\vartheta) \sin\phi \sin\theta + ((\tilde{z}(m) - \tilde{z}(n))\tilde{d}_z - v\tau \cos\vartheta) \cos\theta] \right) \right. \\ & \left. \times \sin\theta \right\} d\phi d\theta \end{aligned} \quad (11)$$

The rotation angles can be selected such that  $(\tilde{x}(m) - \tilde{x}(n))\tilde{d}_x - v\tau \cos\varphi \sin\vartheta = 0$  and  $(\tilde{y}(m) - \tilde{y}(n))\tilde{d}_y - v\tau \sin\varphi \sin\vartheta = 0$ , the expression in (11) is hence simplifies to

$$\begin{aligned} [\mathbf{R}(\tau)]_{m,n} = & \frac{1}{2\pi} \int_0^\pi \int_0^\pi \left\{ \exp \left( j \frac{2\pi}{\lambda} \|\mathbf{d}_m - \mathbf{d}_n - \tau\mathbf{v}\| \cos\theta \right) \sin\theta \right\} d\phi d\theta \\ \stackrel{(a)}{=} & \frac{\sin\left(\frac{2\pi}{\lambda} \|\mathbf{d}_m - \mathbf{d}_n - \tau\mathbf{v}\| \right)}{\frac{2\pi}{\lambda} \|\mathbf{d}_m - \mathbf{d}_n - \tau\mathbf{v}\|} \end{aligned} \quad (12)$$

where (a) follows by employing Euler's formula.

Proposition 1 reveals that the joint spatial-temporal correlation among RIS elements is characterized by a 4D (the 3D space plus the time dimension) sinc function, from which the following observations can be drawn. First, the correlation is minimal only for some element spacing, instead of between any two elements, thus the i.i.d. Rayleigh fading model is not applicable in such a system, which is consistent with the conclusions made in [20], [25]. Second, distinct from the situation in [20] without temporal correlation statistics, the correlation in (9) depends on the spatial and temporal domains jointly. More specifically, the correlation is low when  $\|\mathbf{d}_m - \mathbf{d}_n - \tau\mathbf{v}\|$  is equal or close to integer multiples of half-wavelength, and reaches the maximum when  $\mathbf{d}_m - \mathbf{d}_n = \tau\mathbf{v}$ , i.e., it is possible for two relatively distant elements to have high spatial-temporal correlation if the difference of their coordinate vectors aligns with the speed vector multiplied by the time interval. Physically, the  $m$ -th element arrives at the current location of the  $n$ -th element after traveling time interval  $\tau$ , hence it "sees" the same channel as the  $n$ -th element at the current time instant. This observation is quite different from the spatial-only case where high correlation is usually yielded merely by closely-spaced elements. Additionally, the rank of the channel can be characterized by the non-zero eigenvalues. The i.i.d. Rayleigh fading channel has identical non-zero eigenvalues whose amount equals the number of antenna elements deployed, while the correlated channel has fewer dominant eigenvalues and smaller rank.

#### IV. NON-ISOTROPIC SCATTERING

In this section, we investigate the small-scale spatial-temporal correlation model for the more realistic non-isotropic environment. Based on the statistical spatial channel model built upon the extensive propagation measurements conducted by NYU WIRELESS at mmWave frequencies in dense urban environments [15], [21]–[23], the azimuth AoA within a spatial lobe is normally distributed with a standard deviation of  $\sigma_\phi = 7.5^\circ$ , while the zenith AoA obeys the (wrapped) Laplace distribution with a standard deviation of  $\sigma_\theta = 6.0^\circ$ . Since the average number of spatial lobes is between 1 and 2 statistically [15], we assume one spatial lobe hereupon. As a result,

the angular distribution  $f(\phi, \theta)$  can be described by

$$\begin{aligned}
f(\phi, \theta) &= \frac{1}{\sigma_\phi \sqrt{2\pi}} e^{-\frac{1}{2} \left( \frac{\phi - \mu_\phi}{\sigma_\phi} \right)^2} \frac{1}{\sqrt{2\sigma_\theta}} e^{-\frac{\sqrt{2}|\theta - \mu_\theta|}{\sigma_\theta}} \frac{4}{\left[ \operatorname{erf} \left( \frac{\pi - \mu_\phi}{\sigma_\phi \sqrt{2}} \right) - \operatorname{erf} \left( \frac{-\mu_\phi}{\sigma_\phi \sqrt{2}} \right) \right] \left[ 2 - e^{-\frac{\sqrt{2}\mu_\theta}{\sigma_\theta}} - e^{\frac{\sqrt{2}(\mu_\theta - \pi)}{\sigma_\theta}} \right]} \\
&= \frac{2}{\sqrt{\pi} \sigma_\phi \sigma_\theta \left[ \operatorname{erf} \left( \frac{\pi - \mu_\phi}{\sigma_\phi \sqrt{2}} \right) - \operatorname{erf} \left( \frac{-\mu_\phi}{\sigma_\phi \sqrt{2}} \right) \right] \left[ 2 - e^{-\frac{\sqrt{2}\mu_\theta}{\sigma_\theta}} - e^{\frac{\sqrt{2}(\mu_\theta - \pi)}{\sigma_\theta}} \right]} e^{-\frac{1}{2} \left( \frac{\phi - \mu_\phi}{\sigma_\phi} \right)^2 - \frac{\sqrt{2}|\theta - \mu_\theta|}{\sigma_\theta}}, \\
&\theta \in [0, \pi], \varphi \in [0, \pi]
\end{aligned} \tag{13}$$

where  $\mu_\phi$  and  $\mu_\theta$  denote the mean azimuth and zenith AoAs, respectively. Plugging (13) into (6), we obtain the spatial-temporal correlation function at the RIS as

$$\begin{aligned}
[\mathbf{R}(\tau)]_{m,n} &= \frac{2}{\sqrt{\pi} \sigma_\phi \sigma_\theta \left[ \operatorname{erf} \left( \frac{\pi - \mu_\phi}{\sigma_\phi \sqrt{2}} \right) - \operatorname{erf} \left( \frac{-\mu_\phi}{\sigma_\phi \sqrt{2}} \right) \right] \left[ 2 - e^{-\frac{\sqrt{2}\mu_\theta}{\sigma_\theta}} - e^{\frac{\sqrt{2}(\mu_\theta - \pi)}{\sigma_\theta}} \right]} \times \\
&\quad \int_0^\pi \int_0^\pi \left\{ e^{j \frac{2\pi}{\lambda} [(x(m) - x(n))d_x - v\tau \cos \varphi \sin \theta \cos \phi \sin \theta - v\tau \sin \varphi \sin \theta \sin \phi \sin \theta + ((z(m) - z(n))d_z - v\tau \cos \theta) \cos \theta]} \right. \\
&\quad \left. \times e^{-\frac{1}{2} \left( \frac{\phi - \mu_\phi}{\sigma_\phi} \right)^2 - \frac{\sqrt{2}|\theta - \mu_\theta|}{\sigma_\theta}} \right\} d\phi d\theta
\end{aligned} \tag{14}$$

Since (14) is extremely complicated for further analytical derivation, we resort to numerical method to analyze its features.

## V. NUMERICAL RESULTS

Simulations are performed to more thoroughly inspect the small-scale spatial-temporal correlation behavior among the RIS elements. In the simulations,  $L_x = L_z = 4\lambda$ ,  $d_x = d_z = \lambda/8$ , so that  $N_x = 33$ ,  $N = N_x^2$ .

### A. Isotropic Scattering

Fig. 2 illustrates the small-scale spatial correlation among the RIS elements and the channel eigenvalues at a certain time instant, in which the left plot shows the pattern of the spatial-only sinc function. It is evident from Fig. 2 that the small-scale spatial correlation is high when the element spacing is noticeably smaller than half-wavelength. If defining the decorrelation distance  $d_{\text{decor}}$  as the distance where the absolute correlation value drops to  $1/e$  and remains within  $1/e$  afterwards [26], then  $\lambda < d_{\text{decor}} < 1.5\lambda$  in this case. Furthermore, as shown by the right plot of

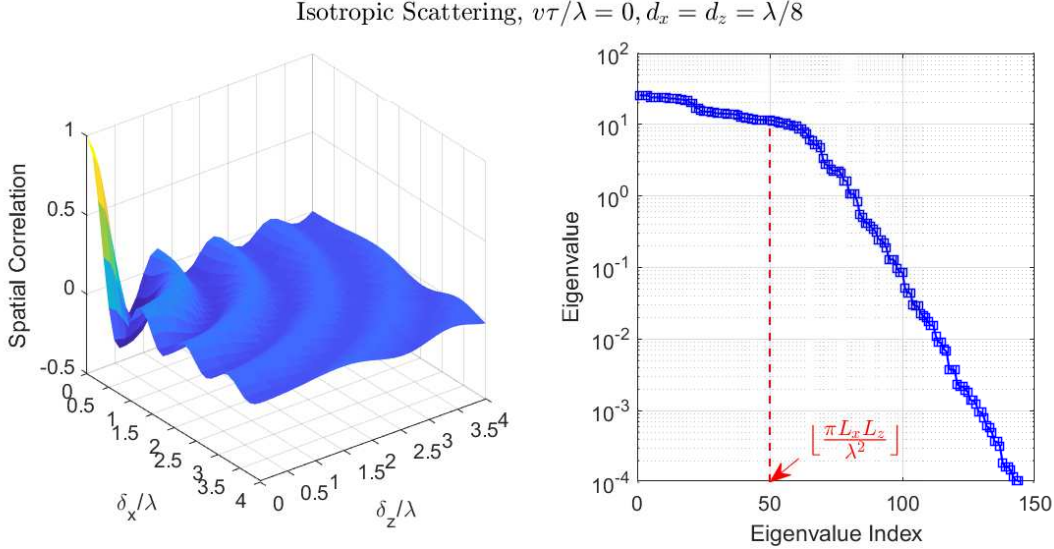


Fig. 2: Spatial correlation among RIS elements (left) and channel eigenvalues (right) associated with isotropic scattering. The adjacent element spacing along the  $x$  and  $z$  directions is both 1/8 of the wavelength.

Fig. 2, the eigenvalues are highly unevenly distributed and the number of dominant eigenvalues is small compared to the total number of elements, unlike the i.i.d. Rayleigh fading channel who would have  $N$  identical eigenvalues. These observations corroborate the fact that the i.i.d. Rayleigh fading model should not be employed for the RIS even in an isotropic scattering environment [7], [20], [25]. In fact, the rank can be estimated as  $\left\lfloor \frac{\pi L_x L_z}{\lambda^2} \right\rfloor$  for a sufficiently dense and large RIS [7], which equals 50 in this case. The dominant  $\left\lfloor \frac{\pi L_x L_z}{\lambda^2} \right\rfloor$  eigenvalues contain about 82% of the total channel power, and the remaining eigenvalues decay to zero rapidly as evident from the right plot of Fig. 2.

The joint spatial-temporal correlation pattern when the RIS moves along the  $x$  direction is depicted in Fig. 3, where  $\delta_x$  and  $\delta_z$  denote respectively the horizontal and vertical distances in meters between RIS elements, the top horizontal slice manifests the the spatial-only correlation equivalent to the left plot of Fig. 2, while the vertical slices delineate the joint spatial-temporal correlation along the  $x$  direction for multiple samples at the  $z$  direction. As shown by the vertical slice at  $\delta_z/\lambda = 0$ , the strongest correlation occurs when  $\delta_x/\lambda = v\tau/\lambda$ , and generally decreases accompanied with oscillation, as precisely described by the sinc function in (9). If collectively looking at the correlation pattern across multiple  $z$  positions at  $\delta_x/\lambda = 4$ , we can see that it is also sinc-like behavior which resembles that of the top horizontal slice, indicating the equivalence

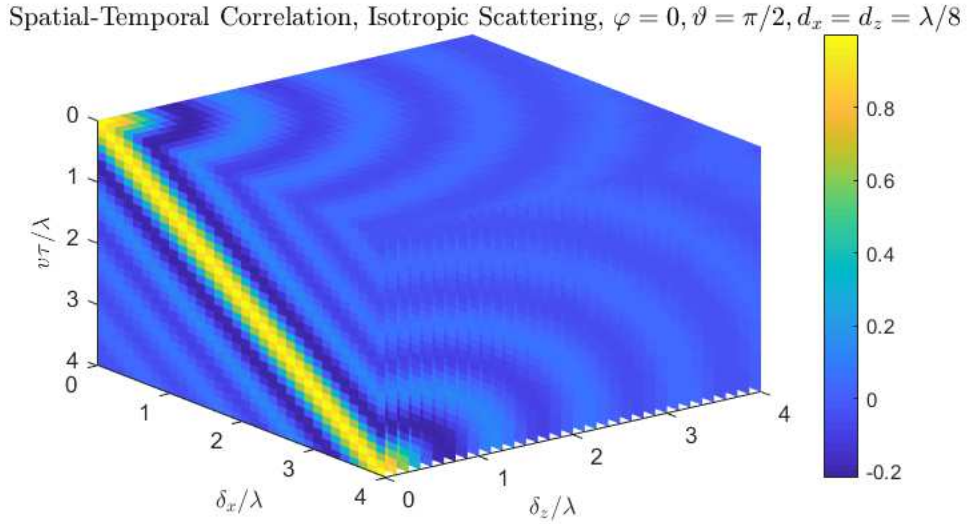


Fig. 3: Joint spatial-temporal correlation among RIS elements associated with isotropic scattering. The adjacent element spacing along the  $x$  and  $z$  directions is both 1/8 of the wavelength, and the RIS moving direction is along the  $x$  axis.

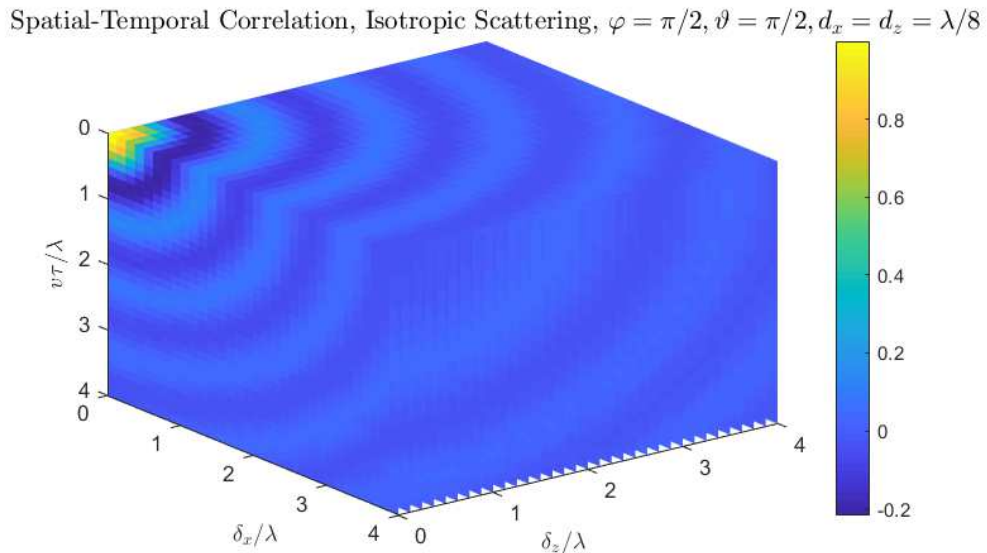


Fig. 4: Joint spatial-temporal correlation among RIS elements associated with isotropic scattering. The adjacent element spacing along the  $x$  and  $z$  directions is both 1/8 of the wavelength, and the RIS moving direction is along the  $y$  axis.

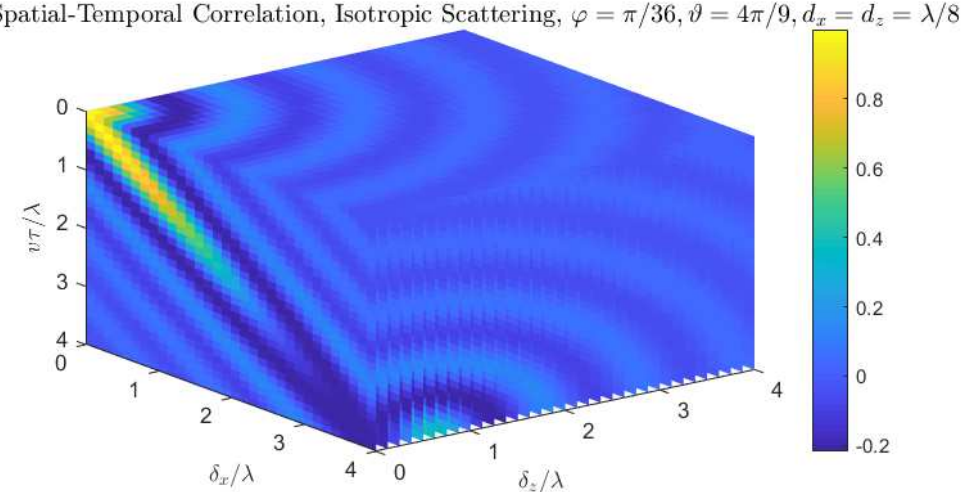


Fig. 5: Joint spatial-temporal correlation among RIS elements associated with isotropic scattering. The adjacent element spacing along the  $x$  and  $z$  directions is both  $1/8$  of the wavelength, and the RIS moving direction is  $\varphi = \pi/36, \vartheta = 4\pi/9$ .

between spatial and temporal shifts, i.e., the correlation distribution at  $\delta_x/\lambda = 0$  and  $v\tau/\lambda = 0$  is equivalent to that at  $\delta_x/\lambda = 4$  and  $v\tau/\lambda = 4$  if the motion direction of the RIS aligns with the  $x$  axis. Due to the rotational invariant resultant from the isotropy nature of the scattering, it is anticipated that the correlation pattern remains the same if the RIS moves along the  $z$  direction with an exchange of  $\delta_x/\lambda$  and  $\delta_z/\lambda$  axes in Fig. 3.

Fig. 4 displays the spatial-temporal correlation when the motion direction of the RIS is perpendicular to its surface. As evident from Fig. 4, the temporal correlation matches the spatial correlation if  $v\tau/\lambda = \delta_x/\lambda$  or  $v\tau/\lambda = \delta_z/\lambda$ , in other words, there is no extra correlation induced by the movement of the RIS. This is because the moving direction is normal to the RIS hence incurring no correlation among the RIS elements. A more general case with the moving angles  $\varphi = 5^\circ, \vartheta = 80^\circ$  is demonstrated in Fig. 5, which shows that the joint spatial-temporal correlation bears a resemblance to a weighted combination of the correlation patterns in Figs. 3 and 4, since the motion direction can be regarded as a linear combination of the orthogonal directions in those two figures.

### B. Non-isotropic Scattering

Without loss of generality, we set the mean azimuth and zenith AoAs of the spatial lobe as  $\mu_\phi = 40^\circ$  and  $\mu_\theta = 80^\circ$ , respectively, in (14). Fig. 6 illustrates the spatial correlation at a

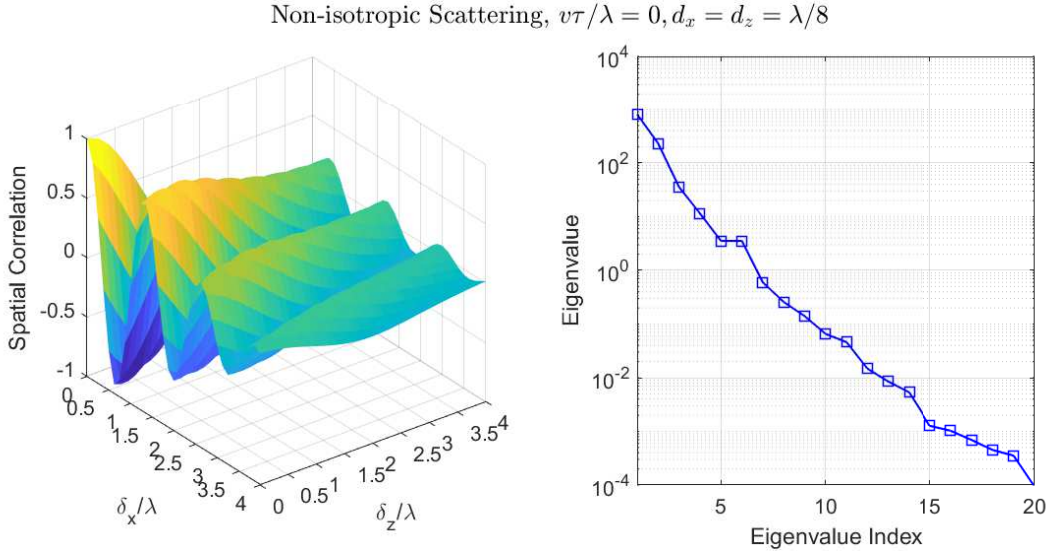


Fig. 6: Spatial correlation among RIS elements (left) and channel eigenvalues (right) associated with non-isotropic scattering. The adjacent element spacing along the  $x$  and  $z$  directions is both 1/8 of the wavelength.

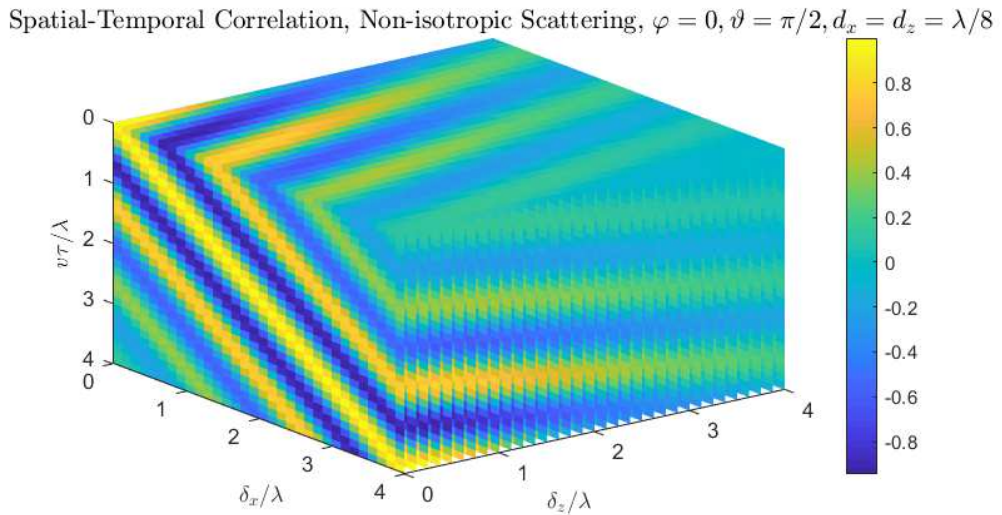


Fig. 7: Joint spatial-temporal correlation among RIS elements associated with non-isotropic scattering. The adjacent element spacing along the  $x$  and  $z$  directions is both 1/8 of the wavelength, and the RIS moving direction is along the  $x$  axis.

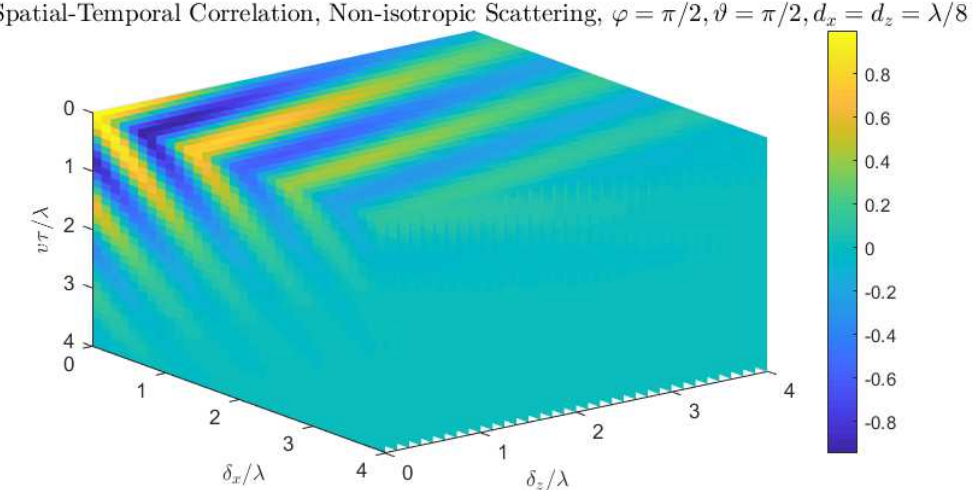


Fig. 8: Joint spatial-temporal correlation among RIS elements associated with non-isotropic scattering. The adjacent element spacing along the  $x$  and  $z$  directions is both  $1/8$  of the wavelength, and the RIS moving direction is along the  $y$  axis.

certain time instant and the corresponding eigenvalues of the channel. It can be seen that the correlation pattern is asymmetric with respect to the diagonal of the RIS, which is expected since the incoming electromagnetic waves are not symmetric about the normal direction of the RIS. The maximum decorrelation distance  $d_{\text{decor}}$  falls in between about  $2.5\lambda$  and  $3\lambda$ , obviously larger than the isotropic scattering case in Fig. 2. More importantly, the dominant eigenvalues are significantly fewer than those for the isotropic scattering case in Fig. 2. For instance, there are 50 dominant eigenvalues that contribute to around 82% of the total channel power under isotropic scattering, while the largest two eigenvalues under non-isotropic scattering herein already occupy about 95% of the total channel power, owing to the relatively concentrated angular distribution hence more severe correlation among RIS elements. This observation sheds light on channel estimation for RIS, i.e., it is likely to be sufficient to estimate only the few dominant eigen-channels.

The non-isotropic scattering counterpart of Figs. 3 and 4 are provided in Figs. 7 and 8, respectively. As observed from Fig. 7, the highest correlation still appears when  $\delta_x/\lambda = v\tau/\lambda$  when the RIS moves in parallel with the  $x$  axis, but the overall correlation pattern does not obey the sinc function any more, with more intense fluctuation in the correlation values. Similarly, Fig. 8 implies that additional temporal correlation does occur even when the motion direction is

perpendicular to the RIS, which is ascribed to the non-isotropy of the arriving electromagnetic waves.

## VI. CONCLUSION

In this paper, we have derived a tractable analytical expression for the joint small-scale spatial-temporal correlation among the elements of a moving RIS in the isotropic scattering environment, and investigated the correlation behavior under non-isotropic scattering using a realistic 3D angular distribution obtained from real-world mmWave propagation measurements. The joint spatial-temporal correlation under isotropic scattering can be modeled by a 4D sinc function. For non-isotropic scattering, the stationary spatial correlation is generally stronger with more fluctuation, leading to substantially fewer dominant eigenvalues thus lower rank, as compared to the isotropic scattering case, and the joint spatial-temporal correlation exhibits more variation as well. The contributions and observations in this paper can provide enlightenment on the proper exploitation of the RIS technology.

## REFERENCES

- [1] T. L. Marzetta, “Noncooperative cellular wireless with unlimited numbers of base station antennas,” *IEEE Transactions on Wireless Communications*, vol. 9, no. 11, pp. 3590–3600, 2010.
- [2] H. Yan and I. Lu, “Asynchronous reception effects on distributed Massive MIMO-OFDM system,” *IEEE Transactions on Communications*, vol. 67, no. 7, pp. 4782–4794, Jul. 2019.
- [3] H. Yan and H. Yang, “Pilot length and channel estimation for Massive MIMO IoT systems,” *IEEE Transactions on Vehicular Technology*, vol. 69, no. 12, pp. 15 532–15 544, Dec. 2020.
- [4] H. Yan, A. Ashikhmin, and H. Yang, “Optimally supporting IoT with cell-free Massive MIMO,” in *GLOBECOM 2020 - 2020 IEEE Global Communications Conference*, 2020, pp. 1–6.
- [5] ———, “Can Massive MIMO support URLLC?” in *2021 IEEE 93rd Vehicular Technology Conference (VTC2021-Spring)*, 2021.
- [6] T. L. Marzetta, “Super-directive antenna arrays: Fundamentals and new perspectives,” in *2019 53rd Asilomar Conference on Signals, Systems, and Computers*, 2019, pp. 1–4.
- [7] A. Pizzo, T. L. Marzetta, and L. Sanguinetti, “Spatially-stationary model for Holographic MIMO small-scale fading,” *IEEE Journal on Selected Areas in Communications*, vol. 38, no. 9, pp. 1964–1979, Sep. 2020.
- [8] C. Huang, S. Hu, G. C. Alexandropoulos, A. Zappone, C. Yuen, R. Zhang, M. D. Renzo, and M. Debbah, “Holographic MIMO surfaces for 6G wireless networks: Opportunities, challenges, and trends,” *IEEE Wireless Communications*, vol. 27, no. 5, pp. 118–125, Oct. 2020.
- [9] C. L. Holloway, E. F. Kuester, J. A. Gordon, J. O’Hara, J. Booth, and D. R. Smith, “An overview of the theory and applications of metasurfaces: The two-dimensional equivalents of metamaterials,” *IEEE Antennas and Propagation Magazine*, vol. 54, no. 2, pp. 10–35, 2012.
- [10] S. Sun *et al.*, “Wide-incident-angle chromatic polarized transmission on trilayer silver/dielectric nanowire gratings,” *Journal of the Optical Society of America B*, vol. 31, no. 5, pp. 1211–1216, May 2014.

- [11] E. Basar, M. Di Renzo, J. De Rosny, M. Debbah, M. Alouini, and R. Zhang, "Wireless communications through reconfigurable intelligent surfaces," *IEEE Access*, vol. 7, pp. 116 753–116 773, Aug. 2019.
- [12] S. Sun and H. Yan, "Channel estimation for reconfigurable intelligent surface-assisted wireless communications considering Doppler effect," *IEEE Wireless Communications Letters*, pp. 1–1, 2020.
- [13] S. Hu, F. Rusek, and O. Edfors, "Beyond massive mimo: The potential of data transmission with large intelligent surfaces," *IEEE Transactions on Signal Processing*, vol. 66, no. 10, pp. 2746–2758, May 2018.
- [14] M. Shafi, J. Zhang, H. Tataria, A. F. Molisch, S. Sun, T. S. Rappaport, F. Tufvesson, S. Wu, and K. Kitao, "Microwave vs. millimeter-wave propagation channels: Key differences and impact on 5G cellular systems," *IEEE Communications Magazine*, vol. 56, no. 12, pp. 14–20, 2018.
- [15] S. Sun, T. S. Rappaport, M. Shafi, P. Tang, J. Zhang, and P. J. Smith, "Propagation models and performance evaluation for 5G millimeter-wave bands," *IEEE Transactions on Vehicular Technology*, vol. 67, no. 9, pp. 8422–8439, Sep. 2018.
- [16] S. Sun, T. S. Rappaport, M. Shafi, and H. Tataria, "Analytical framework of hybrid beamforming in multi-cell millimeter-wave systems," *IEEE Transactions on Wireless Communications*, vol. 17, no. 11, pp. 7528–7543, Nov. 2018.
- [17] S. Sun, T. S. Rappaport, T. A. Thomas, and A. Ghosh, "A preliminary 3D mm wave indoor office channel model," in *2015 International Conference on Computing, Networking and Communications (ICNC)*, 2015, pp. 26–31.
- [18] W. Tang, M. Z. Chen, X. Chen, J. Y. Dai, Y. Han, M. Di Renzo, Y. Zeng, S. Jin, Q. Cheng, and T. J. Cui, "Wireless communications with reconfigurable intelligent surface: Path loss modeling and experimental measurement," *IEEE Transactions on Wireless Communications*, vol. 20, no. 1, pp. 421–439, 2021.
- [19] E. Basar and I. Yildirim, "SimRIS channel simulator for reconfigurable intelligent surface-empowered communication systems," in *2020 IEEE Latin-American Conference on Communications (LATINCOM)*, 2020, pp. 1–6.
- [20] E. Björnson and L. Sanguinetti, "Rayleigh fading modeling and channel hardening for reconfigurable intelligent surfaces," *IEEE Wireless Communications Letters*, pp. 1–1, 2020.
- [21] T. S. Rappaport, S. Sun, R. Mayzus, H. Zhao, Y. Azar, K. Wang, G. N. Wong, J. K. Schulz, M. Samimi, and F. Gutierrez, "Millimeter wave mobile communications for 5G cellular: It will work!" *IEEE Access*, vol. 1, pp. 335–349, May 2013.
- [22] S. Sun and T. S. Rappaport, "Wideband mmWave channels: Implications for design and implementation of adaptive beam antennas," in *2014 IEEE MTT-S International Microwave Symposium (IMS2014)*, 2014, pp. 1–4.
- [23] S. Sun, G. R. MacCartney, and T. S. Rappaport, "A novel millimeter-wave channel simulator and applications for 5G wireless communications," in *2017 IEEE International Conference on Communications (ICC)*, 2017, pp. 1–7.
- [24] 3GPP TR 38.901, V16.1.0, "Study on channel model for frequencies from 0.5 to 100 GHz," Dec. 2019.
- [25] A. Pizzo, T. Marzetta, and L. Sanguinetti, "Holographic MIMO communications under spatially-stationary scattering." [Online]. Available: <https://arxiv.org/abs/2012.07389>.
- [26] S. Sun, H. Yan, G. R. MacCartney, and T. S. Rappaport, "Millimeter wave small-scale spatial statistics in an urban microcell scenario," in *2017 IEEE International Conference on Communications (ICC)*, 2017, pp. 1–7.